Visible photoelectrochemical water splitting into H_2 and O_2 in a dye-sensitized photoelectrosynthesis cell

Leila Alibabaei[a], Benjamin D. Sherman[a], Michael R. Norris[b], M. Kyle Brennaman[a], and Thomas J. Meyer[a,1]

[a]Department of Chemistry, University of North Carolina at Chapel Hill, Chapel Hill, NC 27599; and [b]Department of Chemistry, University of Washington, Seattle, WA 98195

Contributed by Thomas J. Meyer, March 31, 2015 (sent for review January 28, 2015; reviewed by James K. McCusker)

A hybrid strategy for solar water splitting is exploited here based on a dye-sensitized photoelectrosynthesis cell (DSPEC) with a mesoporous SnO_2/TiO_2 core/shell nanostructured electrode derivatized with a surface-bound Ru(II) polypyridyl-based chromophore–catalyst assembly. The assembly, $[(4,4'\text{-}(PO_3H_2)_2bpy)_2Ru(4\text{-}Mebpy\text{-}4'\text{-}bimpy)Ru(tpy)(OH_2)]^{4+}$ ($[Ru_a^{II}\text{-}Ru_b^{II}\text{-}OH_2]^{4+}$, combines both a light absorber and a water oxidation catalyst in a single molecule. It was attached to the TiO_2 shell by phosphonate-surface oxide binding. The oxide-bound assembly was further stabilized on the surface by atomic layer deposition (ALD) of either Al_2O_3 or TiO_2 overlayers. Illumination of the resulting fluorine-doped tin oxide (FTO)$|SnO_2/TiO_2|\text{-}[Ru_a^{II}\text{-}Ru_b^{II}\text{-}OH_2]^{4+}$ (Al_2O_3 or TiO_2) photoanodes in photoelectrochemical cells with a Pt cathode and a small applied bias resulted in visible-light water splitting as shown by direct measurements of both evolved H_2 and O_2. The performance of the resulting DSPECs varies with shell thickness and the nature and extent of the oxide overlayer. Use of the SnO_2/TiO_2 core/shell compared with *nano*ITO/TiO_2 with the same assembly results in photocurrent enhancements of ∼5. Systematic variations in shell thickness and ALD overlayer lead to photocurrent densities as high as 1.97 mA/cm^2 with 445-nm, ∼90-mW/cm^2 illumination in a phosphate buffer at pH 7.

dye-sensitized photoelectrosynthesis cell | water oxidation | core/shell

Although promising, significant challenges remain in the search for successful strategies for artificial photosynthesis by water splitting into oxygen and hydrogen or reduction of CO_2 to reduced forms of carbon (1–5). In a dye-sensitized photoelectrosynthesis cell (DSPEC), a wide band gap, nanoparticle oxide film, typically TiO_2, is derivatized with a surface-bound molecular assembly or assemblies for light absorption and catalysis (6–8). In a DSPEC, visible light is absorbed by a chromophore, initiating a series of events that culminate in water splitting: injection, intra-assembly electron transfer, catalyst activation, and electron transfer to a cathode or photocathode for H_2 production. Sun and coworkers have recently demonstrated visible-light–driven water splitting with a coloading approach combining Ru(II) polypyridyl-based light absorbers and catalysts on TiO_2 (9). The efficiency of DSPEC devices is dependent on interfacial dynamics and competing kinetic processes. A major limiting factor is the requirement for accumulating multiple oxidative equivalents at a catalyst site to meet the $4e^-/4H^+$ demands for oxidizing water to dioxygen ($2H_2O - 4e^- - 4H^+ \rightarrow O_2$) in competition with back electron transfer of injected electrons to the oxidized assembly.

One approach to achieving structural control of local electron transfer dynamics at the oxide interface in dye-sensitized devices is by use of nanostructured core/shell electrodes (10–12). In this approach, a mesoporous network of nanoparticles is uniformly coated with a thin oxide overlayer prepared by atomic layer deposition (ALD). We have used core/shell electrodes to demonstrate benzyl alcohol dehydrogenation (13). This approach has also been used to enhance the efficiency of dye-sensitized solar cells (14, 15). Recently, we described the use of a core/shell consisting of an inner core of a nanoparticle transparent conducting oxide, tin-doped indium oxide (*nano*ITO), and a thin outer shell of TiO_2 for water splitting by visible light (16). Derivatization of the *nano*ITO/TiO_2 core/shell electrode by surface binding of the chromophore–catalyst assembly, $[(4,4'\text{-}(PO_3H_2)_2bpy)_2Ru_a(4\text{-}Mebpy\text{-}4'\text{-}bimpy)Ru_b(tpy)(OH_2)]^{4+}$ (**1**; -$[Ru_a^{II}\text{-}Ru_b^{II}\text{-}OH_2]^{4+}$) shown in Fig. 1*A*, provided the basis for a photoanode in a DSPEC application with a Pt cathode for H_2 generation with a small applied bias in an acetate buffer at pH 4.6.

Application of the core/shell structure led to a greatly enhanced efficiency for water splitting compared with mesoscopic, nanoparticle TiO_2 but the per-photon absorbed efficiency of the resulting DSPEC was relatively low and problems arose from long-term instability due to loss of the assembly from the oxide surface in the acetate buffer at pH 4.6. The latter is problematic because the rate of water oxidation is enhanced by added buffer bases, conditions that also enhance the rate of water oxidation (5, 17–24).

Here, we report a second-generation DSPEC based on a core/shell photoanode. It features both greatly enhanced efficiencies for visible-light–driven water splitting and stabilization of surface binding by the assembly. Enhanced efficiencies come from the use of a SnO_2 core in a SnO_2/TiO_2 core/shell structure. SnO_2 has a conduction band potential (E_{CB}) more positive than TiO_2 by ∼0.4 V. Once injection and electron transfer to the SnO_2 core has occurred, an internal potential gradient at the SnO_2/TiO_2 interface is established, inhibiting back electron transfer.

In the second-generation DSPEC, ALD is also used to stabilize oxide surface binding by the phosphonate-derivatized assembly. ALD deposition of overlayers of TiO_2 or Al_2O_3 has been shown to greatly enhance surface stability toward hydrolysis even in strongly basic solutions (25, 26). We show here, for assembly **1** surface-bound to SnO_2/TiO_2, that ALD overlayers of TiO_2 or Al_2O_3 provide both long-term stabilization on the oxide surface at pH 7 in a phosphate buffer, and, as a bonus, incrementally enhanced efficiencies for water splitting (23).

The underlying strategy behind the use of ALD for both core/shell structure and stabilized surface binding is illustrated in Fig. 1*C*. Detailed information about the mechanism and rate of water

Significance

Mesoporous SnO_2/TiO_2 core/shell nanostructured electrodes derivatized with a surface-bound Ru(II) polypyridyl-based chromophore–catalyst assembly are used for water splitting into H_2 and O_2 with visible light in a dye-sensitized photoelectrosynthesis cell. Photocurrents with a small applied bias are among the highest reported. Stabilization of the assembly on the surface of the TiO_2 shell by using atomic layer deposition to deposit overlayers of Al_2O_3 or TiO_2 results in long-term water splitting even in a phosphate buffer at pH 7.

Author contributions: L.A. designed research; L.A. and B.D.S. performed research; B.D.S. and M.R.N. contributed new reagents/analytic tools; L.A., M.K.B., and T.J.M. analyzed data; and L.A. and T.J.M. wrote the paper.

Reviewers included: J.K.M., Michigan State University.

The authors declare no conflict of interest.

[1]To whom correspondence should be addressed. Email: tjmeyer@unc.edu.

This article contains supporting information online at www.pnas.org/lookup/suppl/doi:10.1073/pnas.1506111112/-/DCSupplemental.

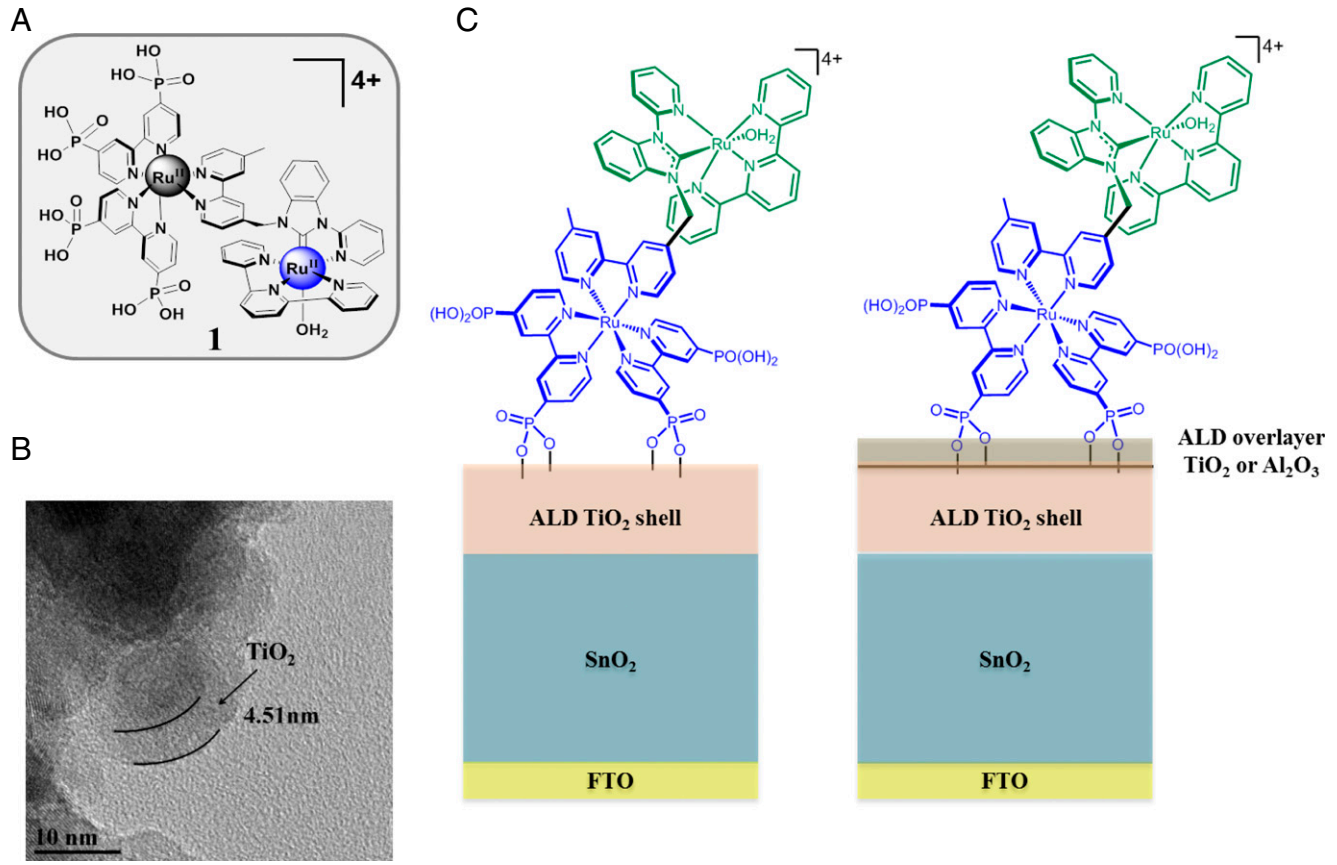

Fig. 1. (*A*) Chemical structure of chromophore–catalyst assembly **1**, -[Ru_a^{II}-Ru_b^{II}-OH_2]$^{4+}$. (*B*) TEM depicting a core/shell nanostructure from 75 ALD cycles of TiO_2 deposited onto SnO_2 films on FTO glass (FTO|SnO_2/TiO_2(4.5 nm)|). (*C*) Cartoon depicting an ALD core/shell electrode surface with and without ALD overlayer stabilization of a surface-bound assembly.

oxidation by the surface-bound assembly is available from a previous publication (27).

Results

Preparation of SnO_2/TiO_2 core/shell structures is described in *SI Text*. A transmission electron micrograph (TEM) is shown in Fig. 1*B* illustrating the core/shell structure prepared by uniformly coating a SnO_2 nanoparticle film with 75 ALD cycles of TiO_2.

Current–time (i–t) profiles were recorded at the photoanode of a photoelectrochemical cell at pH 4.6 with 20 mM acetate/acetic acid buffer or at pH 7 in a 0.1 M phosphate buffer with 0.5 M added $LiClO_4$. The DSPEC cell consisted of a fluorine-doped tin oxide (FTO)|SnO_2/TiO_2|-[Ru_a^{II}-Ru_b^{II}-OH_2]$^{4+}$ core/shell photoanode with a Pt wire as the cathode. Illumination at 445 nm (FWHM 20 nm, ~10 to ~90 mW/cm^2, beam diameter 1 cm) was provided by a Lumencor SPECTRA seven-color solid-state light source.

Fig. 2*A* compares the results of short-term, current density–time DSPEC measurement at *nano*ITO/TiO_2 and SnO_2/TiO_2 core/shell electrodes with a nominal TiO_2 shell thickness of 3.3 with an applied bias of 200 mV vs. normal hydrogen electrode (NHE). As reported previously (16), cell performance is bias-dependent with an applied bias required to maximize photocurrent and H_2 evolution at the cathode.

From the data in Fig. 2*A* and the data summary in Tables S1 and S2, a maximum initial photocurrent density of 0.48 mA/cm^2 was reached for the SnO_2/TiO_2 (3.3-nm) core/shell photoanode, falling to 0.1 mA/cm^2 after 10 s at the end of the initial current spike. The initial photocurrent increased to 0.79 mA/cm^2 with a 0.66-nm overlayer of TiO_2. The initial current spike arises from oxidation of the assembly to its steady-state form -[Ru_a^{III}-Ru_b^{IV} = O]$^{4+}$ and from local capacitance effects (28, 29).

The small dark current at the end of the light-on/light-off cycles is a characteristic feature of DSPECs arising from electron equilibration by back electron transfer through the core/shell network to the partly oxidized, surface-bound assemblies.

Photocurrent comparisons were made after 10 s of 445-nm illumination at the end of the initial current spike at the onset of the plateau current. It is notable that in comparing *nano*ITO/TiO_2 and SnO_2/TiO_2 as core/shells under the same conditions, photocurrent increases of ~5× are observed.

The results of a study of the effect of TiO_2 shell thickness on DSPEC performance for SnO_2/TiO_2 core/shells are summarized in Table 1. These experiments were conducted at pH 7 in a $H_2PO_4^-$/HPO_4^{2-} buffer with [HPO_4^{2-}] ~60 mM. Assembly-surface binding to the TiO_2 shell under these conditions was stabilized by ALD deposition of a 0.55-nm-thick overlayer of Al_2O_3.

The results in Table 1 show that compared with a SnO_2 core, the photocurrent density increases by greater than 30× for SnO_2/TiO_2 core/shells with shell thicknesses from 3.3 to 6.6 nm. The photocurrent density, which is dependent on TiO_2 shell thickness over the range 3.3, 4.5, 6.6 nm, is maximized at 4.5 nm (75 ALD cycles).

There is also a dependence on the number of ALD overlayer stabilization cycles and on the nature of the added overlayer. Based on photocurrent data at pH 4.6 and pH 7 in Table S3 and Fig. S1, photocurrent efficiencies for the assembly-based photoanode, FTO|SnO_2/TiO_2(6.6 nm)|-[Ru_a^{II}-Ru_b^{II}-OH_2]$^{4+}$, were maximized by 0.33- or 0.55-nm-thick ALD overlayers of Al_2O_3 with enhancements greater for Al_2O_3 than for TiO_2. For the TiO_2 overlayers, the

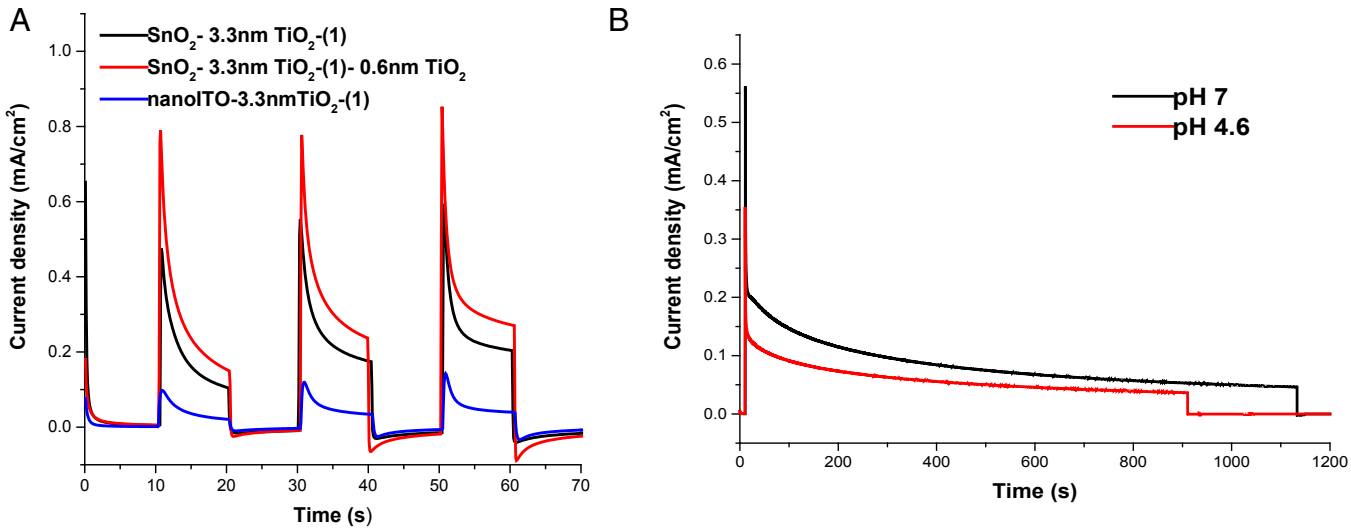

Fig. 2. (*A*) Photocurrent comparisons between SnO_2 and *nano*ITO core/TiO_2 photoanodes, FTO|SnO_2/TiO_2|-[Ru_a^{II}-Ru_b^{II}-OH_2]$^{4+}$ (black) and FTO|*nano*ITO/TiO_2|-[Ru_a^{II}-Ru_b^{II}-OH_2]$^{4+}$ (blue), with 50-cycle ALD TiO_2 shells (3.3 nm) derivatized with **1** with a Pt counterelectrode and 200 mV (vs. NHE) applied bias at pH 4.6 in 0.5 M $LiClO_4$ with 20 mM acetate/acetic acid buffer. The red trace shows the impact of a 10-cycle TiO_2 overlayer on the photocurrent output of the SnO_2 core/shell electrode. (*B*) Photocurrent–time curves for FTO|SnO_2/TiO_2(6.6 nm)|-[Ru_a^{II}-Ru_b^{II}-OH_2]$^{4+}$ with 10 cycles of an added TiO_2 overlayer: 600 mV applied bias vs. NHE in 0.5 M $LiClO_4$ 20 mM in acetic acid/acetate buffer at pH 4.6 (red) and in a 0.1 M $H_2PO_4^-$/HPO_4^{2-} buffer at pH 7 with the ionic strength adjusted to 0.5 M with $NaClO_4$ (black).

enhancement was greater for a TiO_2 overlayer of 0.6 nm compared with 1.2 nm. The highest photocurrents, 1.97 mA/cm^2, were reached with a 0.55-nm overlayer of Al_2O_3. Similar results were obtained for an electrode with an ∼4.5 nm TiO_2 shell as shown by the cyclic voltammetry measurements in the dark and under illumination in Fig. S2.

With no protective overlayer, at pH 4.6 in acetate buffer, loss of the assembly from the surface by hydrolysis is noticeable after a few minutes. At pH 7 in phosphate buffer, the loss is too rapid for current–time measurements. The assembly is stable on the surface under these conditions, however, with ALD-added overlayers of TiO_2 or Al_2O_3. The results of long-term photocurrent measurements on the ALD-stabilized photoanode, FTO|SnO_2/TiO_2(6.6 nm)|-[Ru_a^{II}-Ru_b^{II}-OH_2]$^{4+}$-(0.6 nm)TiO_2, are shown in Fig. 2*B*. These results reveal an impressive enhancement in stability toward surface hydrolysis. A slow decrease in photocurrent is observed with time but it arises from instability toward ligand loss by the Ru (III) form of the chromophore in the assembly (30).

In previous experiments with assembly **1** on core/shell *nano*-ITO/TiO_2, high faradaic efficiencies for H_2 production were reported with O_2 evolution confirmed by a rotating ring disk method (16). In the present study, H_2 and O_2 evolution from FTO|SnO_2/TiO_2(4.5 nm)|-[Ru_a^{II}-Ru_b^{II}-OH_2]$^{4+}$(0.3 nm Al_2O_3) was confirmed by direct Clark-type oxygen and hydrogen microsensor (Unisense) measurements. The sensors, with tip diameters of 1.6 mm, were inserted into the DSPEC cell in the phosphate buffer at pH 7. A schematic is shown in Fig. S3. Current–time plots with 455-nm LED photolysis (46 mW/cm^2) at an applied bias of 600 mV are shown in Fig. 3*A* and evolution curves for the appearance of H_2 and O_2 in Fig. 3*B*. In these experiments, a 600-mV bias was applied between FTO|SnO_2/TiO_2(4.5 nm)|-[Ru_a^{II}-Ru_b^{II}-OH_2]$^{4+}$(0.3 nm Al_2O_3) photoanode and Pt counter in a two-electrode configuration. The faradaic efficiencies for H_2 and O_2 measured after 100 s of photolysis were 57% and 41%, respectively, which are low but typical for these measurements.

The results described here are a notable advance. Introduction of SnO_2/TiO_2 core/shells improves cell efficiencies by a factor of ∼5× (Table S1). Added ALD oxide overlayers stabilize surface binding over extended photolysis periods, even at pH 7 in phosphate buffers. Cell efficiencies can be manipulated by varying the core/shell material and its geometry. Under optimal conditions for a FTO|SnO_2/TiO_2(4.5 nm)|-[Ru_a^{II}-Ru_b^{II}-OH_2]$^{4+}$(0.3 nm Al_2O_3) photoanode, a photocurrent density of 1.97 mA/cm^2 was reached for 445-nm water splitting. The underlying interfacial dynamics for the integrated molecular assembly–oxide device are currently under investigation by transient absorption and photocurrent measurements to assess the kinetic factors required to further increase cell efficiencies.

These results are important in expanding the scope of DSPEC water splitting by manipulating core/shell structure and incorporating ALD overlayer protection toward hydrolysis. Major

Table 1. TiO_2 shell thickness effect on current densities for FTO|SnO_2/TiO_2|-[Ru_a^{II}-Ru_b^{II}-OH_2]$^{4+}$ as a function of TiO_2 shell thickness and 445-nm light intensity with 0.55 nm of Al_2O_3 overlayer

Light intensity at 445 nm (mW/cm^2)	SnO_2/TiO_2(3.3 nm)|-[Ru_a^{II}-Ru_b^{II}-OH_2]$^{4+}$ (0.55 nm Al_2O_3)	SnO_2/TiO_2(4.5 nm)|-[Ru_a^{II}-Ru_b^{II}-OH_2]$^{4+}$ (no overlayer)	SnO_2/TiO_2(4.5 nm)|-[Ru_a^{II}-Ru_b^{II}-OH_2]$^{4+}$ (0.55 nm Al_2O_3)	SnO_2/TiO_2(6.6 nm)|-[Ru_a^{II}-Ru_b^{II}-OH_2]$^{4+}$ (0.55 nm Al_2O_3)	SnO_2|-[Ru_a^{II}-Ru_b^{II}-OH_2]$^{4+}$ (0.55 nm Al_2O_3)
15	0.80	0.93	1.39	1.14	0.04
56	1.04	1.20	1.89	1.78	0.06
86	1.02	1.26	1.97	1.77	0.02

Experiments were performed at room temperature in a $H_2PO_4^-$/HPO_4^{2-} buffer ([HPO_4^{2-}] ∼60 mM) with the ionic strength adjusted to 0.5 with $NaClO_4$ and an external applied bias of 600 mV vs. NHE. The photocurrent densities in the table are reported in mA/cm^2.

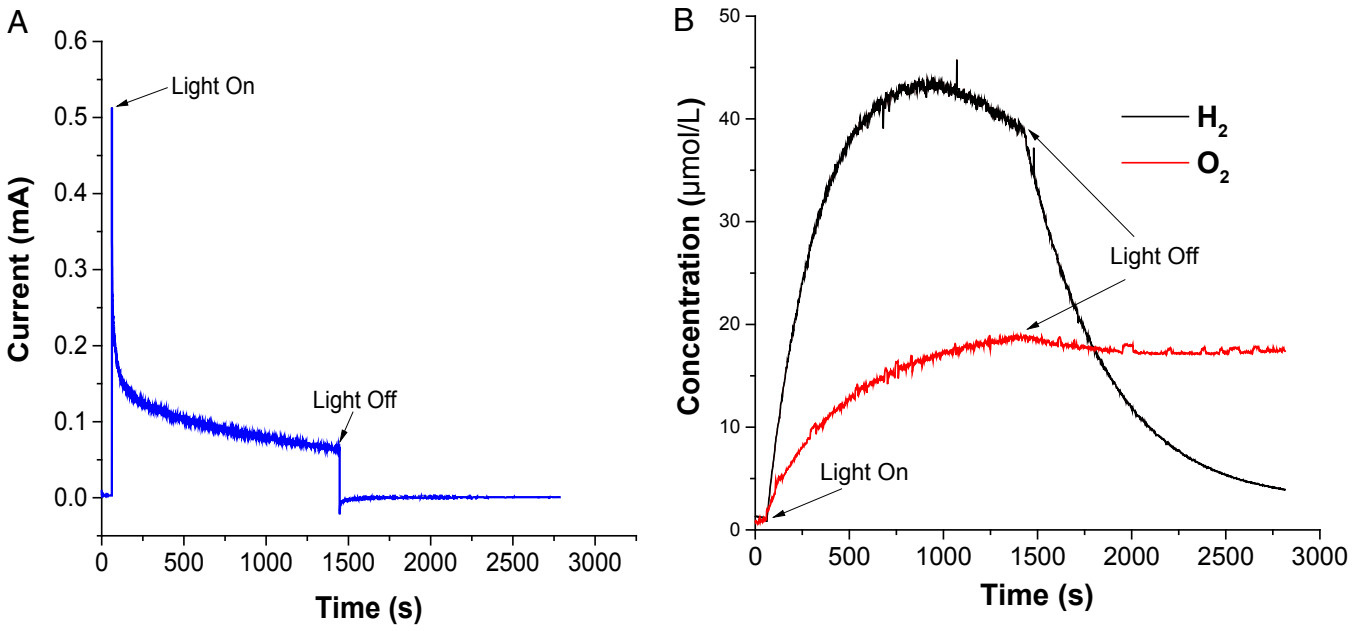

Fig. 3. Photoelectrochemical water splitting by FTO|SnO_2/TiO_2(6.6nm)|-[Ru_a^{II}-Ru_b^{II}-OH_2]$^{4+}$(0.3nmAl_2O_3) with a 600-mV applied bias in a 0.1 M $H_2PO_4^-$/HPO_4^{2-} buffer at pH 7 at room temperature. The bias was applied across the working and counterelectrodes (the experiment was performed in a two-electrode configuration with the counter- and reference leads both connected to the Pt counterelectrode). The ionic strength was adjusted to 0.5 M with $NaClO_4$. Illumination was accomplished with a 455-nm LED at 46.2 mW/cm^2. (*A*) Photocurrent–time trace and (*B*) H_2 and O_2 evolution time traces recorded in concert with the photocurrent trace.

challenges remain in maximizing solar light absorption, achieving higher levels of surface stabilization, and maximizing efficiencies, but the door appears to be open for a systematic exploitation of the DSPEC strategy.

ACKNOWLEDGMENTS. This research was supported solely by the University of North Carolina Energy Frontier Research Center: Center for Solar Fuels, an Energy Frontier Research Center supported by the US Department of Energy, Office of Science, Office of Basic Energy Sciences under Award DE-SC0001011.

1. Concepcion JJ, House RL, Papanikolas JM, Meyer TJ (2012) Chemical approaches to artificial photosynthesis. *Proc Natl Acad Sci USA* 109(39):15560–15564.
2. Alstrum-Acevedo JH, Brennaman MK, Meyer TJ (2005) Chemical approaches to artificial photosynthesis. 2. *Inorg Chem* 44(20):6802–6827.
3. Walter MG, et al. (2010) Solar water splitting cells. *Chem Rev* 110(11):6446–6473.
4. Lewis NS, Nocera DG (2006) Powering the planet: Chemical challenges in solar energy utilization. *Proc Natl Acad Sci USA* 103(43):15729–15735.
5. Faunce TA, et al. (2013) Energy and environment policy case for a global project on artificial photosynthesis. *Energy & Environ Sci* 6(3):695–698.
6. Alibabaei L, et al. (2013) Applications of metal oxide materials in dye sensitized photoelectrosynthesis cells for making solar fuels: Let the molecules do the work. *J Mater Chem A* 1(13):4133–4145.
7. Treadway JA, Moss JA, Meyer TJ (1999) Visible region photooxidation on $TiO_{(2)}$ with a chromophore-catalyst molecular assembly. *Inorg Chem* 38(20):4386–4387.
8. Song W, Chen Z, Brennaman MK, Concepcion J, Meyer TJ (2011) Making solar fuels by artificial photosynthesis. *Pure Appl Chem* 83(4):749–768.
9. Ding X, et al. (2014) Visible light-driven water splitting in photoelectrochemical cells with supramolecular catalysts on photoanodes. *ACS Catalysis* 4(7):2347–2350.
10. Williams VO, et al. (2012) Fast transporting ZnO-TiO_2 coaxial photoanodes for dye-sensitized solar cells based on ALD-modified SiO_2 aerogel frameworks. *ACS Nano* 6(7): 6185–6196.
11. Martinson ABF, et al. (2008) Radial electron collection in dye-sensitized solar cells. *Nano Lett* 8(9):2862–2866.
12. Park K, et al. (2010) Effect of an ultrathin $TiO_{(2)}$ layer coated on submicrometer-sized ZnO nanocrystallite aggregates by atomic layer deposition on the performance of dye-sensitized solar cells. *Adv Mater* 22(21):2329–2332.
13. Song W, et al. (2014) Visible light driven benzyl alcohol dehydrogenation in a dye-sensitized photoelectrosynthesis cell. *J Am Chem Soc* 136(27):9773–9779.
14. Alibabaei L, et al. (2014) Atomic layer deposition of TiO_2 on mesoporous nanoITO: Conductive core-shell photoanodes for dye-sensitized solar cells. *Nano Lett* 14(6): 3255–3261.
15. Chandiran AK, et al. (2013) Low-temperature crystalline titanium dioxide by atomic layer deposition for dye-sensitized solar cells. *ACS Appl Mater Interfaces* 5(8): 3487–3493.
16. Alibabaei L, et al. (2013) Solar water splitting in a molecular photoelectrochemical cell. *Proc Natl Acad Sci USA* 110(50):20008–20013.
17. Moore GF, et al. (2011) A visible light water-splitting cell with a photoanode formed by codeposition of a high-potential porphyrin and an iridium water-oxidation catalyst. *Energy & Environ Sci* 4(7):2389–2392.
18. Lv H, et al. (2012) Polyoxometalate water oxidation catalysts and the production of green fuel. *Chem Soc Rev* 41(22):7572–7589.
19. Gao Y, et al. (2013) Visible light driven water splitting in a molecular device with unprecedentedly high photocurrent density. *J Am Chem Soc* 135(11):4219–4222.
20. Brimblecombe R, Koo A, Dismukes GC, Swiegers GF, Spiccia L (2010) Solar driven water oxidation by a bioinspired manganese molecular catalyst. *J Am Chem Soc* 132(9):2892–2894.
21. Youngblood WJ, et al. (2009) Photoassisted overall water splitting in a visible light-absorbing dye-sensitized photoelectrochemical cell. *J Am Chem Soc* 131(3):926–927.
22. Chen Z, et al. (2010) Concerted O atom-proton transfer in the O-O bond forming step in water oxidation. *Proc Natl Acad Sci USA* 107(16):7225–7229.
23. Vannucci AK, et al. (2013) Crossing the divide between homogeneous and heterogeneous catalysis in water oxidation. *Proc Natl Acad Sci USA* 110(52):20918–20922.
24. Tamaki Y, Vannucci AK, Dares CJ, Binstead RA, Meyer TJ (2014) One-electron activation of water oxidation catalysis. *J Am Chem Soc* 136(19):6854–6857.
25. Hanson K, et al. (2013) Stabilization of [Ru(bpy)2(4,4′-(PO3H2)bpy)]2+ on mesoporous TiO2 with atomic layer deposition of Al_2O_3. *Chem Mater* 25(1):3–5.
26. Hanson K, Losego MD, Kalanyan B, Parsons GN, Meyer TJ (2013) Stabilizing small molecules on metal oxide surfaces using atomic layer deposition. *Nano Lett* 13(10): 4802–4809.
27. Norris MR, Concepcion JJ, Fang Z, Templeton JL, Meyer TJ (2013) Low-overpotential water oxidation by a surface-bound ruthenium-chromophore-ruthenium-catalyst assembly. *Angew Chem Int Ed Engl* 52(51):13580–13583.
28. Swierk JR, McCool NS, Saunders TP, Barber GD, Mallouk TE (2014) Effects of electron trapping and protonation on the efficiency of water-splitting dye-sensitized solar cells. *J Am Chem Soc* 136(31):10974–10982.
29. Zhao Y, et al. (2012) Improving the efficiency of water splitting in dye-sensitized solar cells by using a biomimetic electron transfer mediator. *Proc Natl Acad Sci USA* 109(39): 15612–15616.
30. Hyde JT, et al. (2015) Electrochemical instability of phosphonate-derivatized RuIII polypyridyl complexes on metal oxide surfaces. *ACS Appl Mater Interfaces*, 10.1021/acsami.5b01000.